

Carbon dioxide absorption in water/nanofluid by a symmetric amine-based nanodendritic adsorbent

M. Arshadi^a, H. Taghvaei^{b,*}, M.K. Abdolmaleki^a, M. Lee^a, H. Eskandarloo^a, A. Abbaspourrad^{a,*}

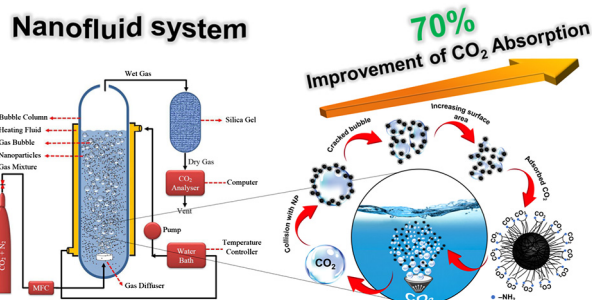
^a Department of Food Science, College of Agriculture and Life Sciences, Cornell University, 243 Stocking Hall, Ithaca, NY 14853, United States

^b Department of Chemical Engineering, Shiraz University, Shiraz 71345, Iran

HIGHLIGHTS

- Several modified Fe_3O_4 nanoparticles were used for CO_2 absorption in water/nanofluid.
- The hydrophobic and hydrophilic reagents coated on the magnetite Fe_3O_4 core-shell.
- The nanodendritic adsorbent indicated the highest enhancement of CO_2 absorption (70%).
- $\text{Fe}_3\text{O}_4@\text{SiO}_2\text{-SNH}_2$ retains CO_2 capturing even after 5 absorption/regeneration cycles.

GRAPHICAL ABSTRACT



ARTICLE INFO

Keywords:

Nanofluidic
Dendritic
Water
 CO_2 absorption
Nanoparticle

ABSTRACT

Serious and immediate action is needed to reduce carbon emissions and prevent catastrophic global climate change. In this work, we investigate the enhancement of CO_2 absorption in water by preparing and adding different types of modified Fe_3O_4 nanoparticles to a water-base fluid, creating a nanofluid system that has gained increasing interest over the last decade. The nanoabsorbents are prepared by using different inorganic and organic reagents; tetraethyl orthosilicate (TEOS), (3-Aminopropyl) triethoxysilane (APTES) and diethylenetriamine. These coat the as-synthesized, magnetite Fe_3O_4 core-shell nanoparticles resulting in a symmetric, amine-based nanodendritic CO_2 adsorbent. These reagents were chosen due to their range of various functional groups and hydrophobic or hydrophilic nature, as well as to assess their effect on the absorption of CO_2 . In addition to evaluating the prepared nanofluidic system (nanoparticle/water nanofluids), we also studied the effects of nanoparticle loading, hydrophilicity, the quantity of nanoparticles, reaction temperature, and absorption time on the CO_2 absorption. The nanodendritic adsorbent, with a high density of symmetric amine functional sites and hydrophilicity ($\text{Fe}_3\text{O}_4@\text{SiO}_2\text{-SNH}_2$), showed the highest enhancement of CO_2 absorption (70%) in comparison to the water-based solution, which is higher than that of most reported nanofluidic systems. $\text{Fe}_3\text{O}_4@\text{SiO}_2\text{-SNH}_2$ also retains its performance even after being regenerated for 5 absorption cycles, losing only 3% of its absorption efficiency over this period. Finally, the significant CO_2 absorption, high recyclability under low temperature, and mild regeneration in a water-based nanofluid, as a “green” solvent, make this nanofluidic system a unique candidate for atmospheric CO_2 capture.

* Corresponding authors.

E-mail addresses: Taghvaei.h@shirazu.ac.ir (H. Taghvaei), Alireza@cornell.edu (A. Abbaspourrad).

1. Introduction

The increase of carbon dioxide (CO_2) emissions from the burning of fossil fuels is considered the primary cause of global warming. Prior to the industrial revolution, the atmospheric concentration of CO_2 was ~ 280 ppm, while at present it is nearly ~ 400 ppm. To mitigate the effects of climate change, it is pivotal to control the amount of CO_2 in the atmosphere. This means not only decreasing emissions by diminishing our reliance on fossil fuels, but also developing efficient techniques of capturing and storing CO_2 [1,2].

Having a double bond between oxygen and carbon in CO_2 makes it a highly thermodynamically and chemically stable gas, and as a result, it is a difficult molecule to decompose. Current methods of CO_2 capture include those based on membranes, adsorption, cryogenic techniques, absorption, and chemical looping [3,4]. The main techniques used for CO_2 capture at the source in large-scale industrial applications are based on chemical and physical absorption processes that rely on various solvents as absorbents, such as diethanolamine (DEA) [5], poly(ethylene oxide) (PEG400) [6], methanol [7], ethanol and water [8]. The type of solvents used are the essential component to assess the CO_2 absorption efficiency [5]. Present technologies are mostly based on aqueous alkanolamine media which can capture a portion of the CO_2 present in fuel combustion gases [9,10]. Contrary to commercial applications, the amine-based sorbents result in a considerable capital cost and energy penalty [11,12]. For instance, in a coal-fired power plant, which has lower CO_2 capture costs than natural gas-fired combined cycle [13], use of the current monoethanolamine (MEA) capture technology leads to a 25–40% loss of the overall thermal efficiency and a 70–100% enhancement in the electricity expenses [14]. This is due to the necessity to cool the gas flue in industrial sources lowering the evaporation level of the aminated molecules and reducing the corrosive nature of the carbon dioxide absorbing fluid. In addition, amine-based sorbents consume high amounts of energy during thermal desorption because of strong chemical reactions [11]. These problems can be mitigated by using novel, blended amines with desirable chemical and physical properties such as piperazine (PZ)/4-hydroxy-1-methylpiperidine (HMPD) [15], 1-dimethylamino-2-propanol (1DMA2P) [16] and blended MEA-DEA solvent [17]. Liu et al. studied the CO_2 absorption behavior in the MEA-DEA blend which showed that the addition of DEA into MEA system improves disadvantages of MEA on regeneration heat, degradation, and corrosivity [17].

From another standpoint, amine-based processes show a high absorption rate at atmospheric pressure. Consequently, these types of sorbents are suitable for capturing a portion of the CO_2 present in processes which are performed at atmospheric pressure, such as post combustion processes [9,10]. It should be noted that many energy generation processes operate at high pressure, as in power generation using the gasification of fossil fuels in integrated gasification combined cycle [18,19]. This process converts coal, biomass, heavy petroleum residues and other fossil fuels into pressurized synthesis gas using a high-pressure gasifier. The high-pressure syngas formed in the gasification section is used as fuel for the gas turbine in the combined cycle and should become free of carbon dioxide before combustion.

Pre-combustion syngas cleanup at high pressure requires the study of the advanced CO_2 absorbents in the nontoxic and green solvent, which can absorb CO_2 physically or with hybrid physical and chemical sorption characteristics. Moreover, using physical or hybrid sorbents can be effective in minimizing the energy penalty of CO_2 capturing processes [20]. The combination of solvents with nanoparticles, as nanofluid solvents, for CO_2 absorption could greatly enhance the absorption of CO_2 and decrease energy costs [21]. First proposed by Choi [22], the idea of nanofluid system by spreading the nano-powder (1–100 nm), such as nanoparticles, nanofibers, nanosheets, droplets, nanotubes, or nanowires (nanorods), into aqueous or non-aqueous soluble liquids. A vast number of metallic (Al_2O_3 , Fe_3O_4 , SiO_2 and TiO_2) and non-metallic (single and multi-walled carbon nanotubes)

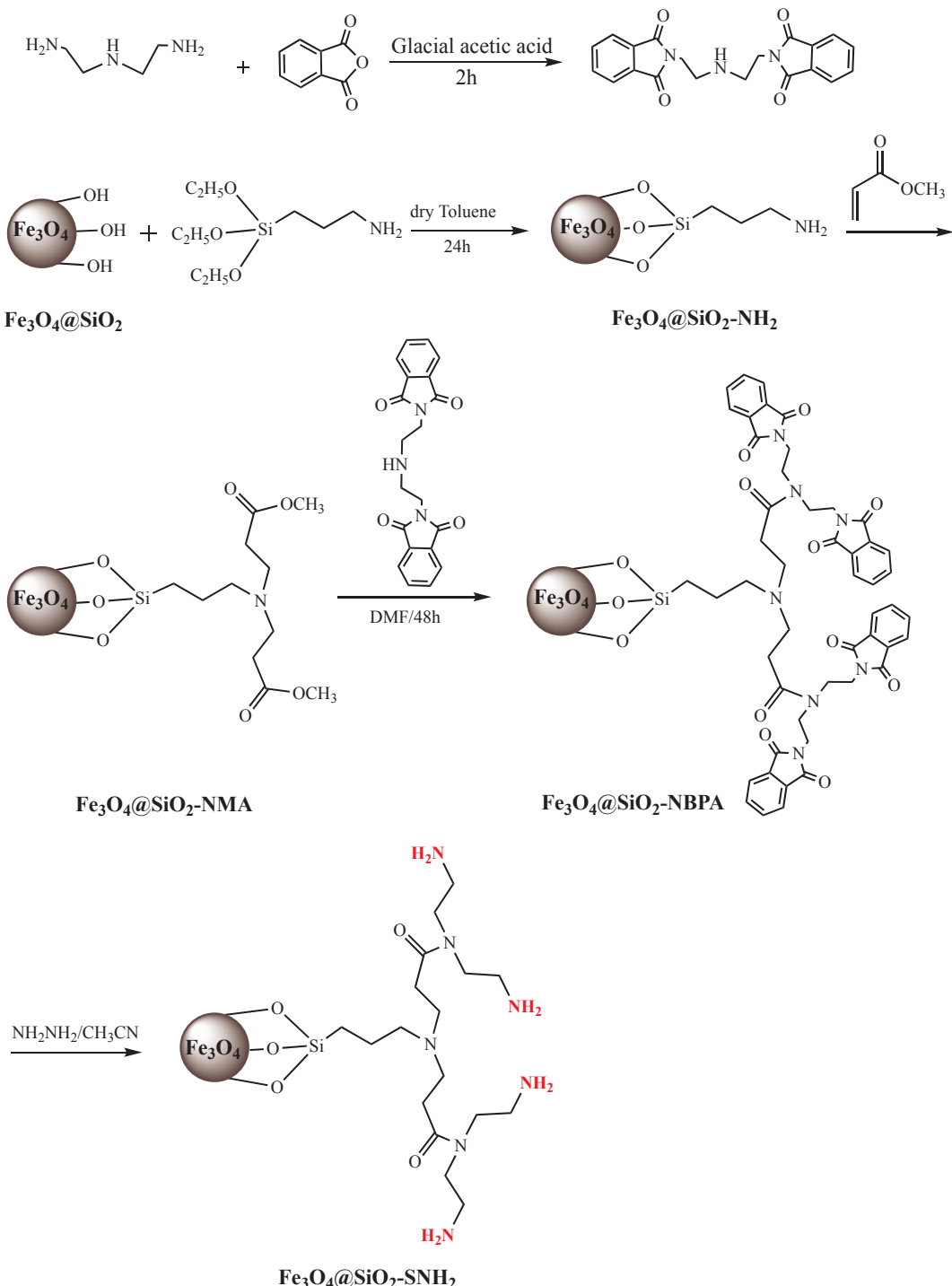
nanofluids can be used to capture CO_2 [23]. Due to the high surface area of the nanoparticles, even including a slight quantity of nanomaterials into the nanofluid solution can significantly enhance the stability, heat and mass transfer performance, and thermal efficiency [24]. Moreover, the nanoparticles can interact with bubbles present in the fluid to make smaller bubbles, which results in enhanced mass transfer through the bubble absorption process [5].

Thus, using nanofluids is a subject of interest for developing advanced systems for increasing the CO_2 absorption. However, one of the major problems associated with the preparation and application of nanofluids is the chemical stability and water dispersibility of the nanoparticles in the host liquid. Ultrasonication is a common method to disperse nanoparticles; however, the resulting nanofluids are typically only stable for a few days and the process is ineffective [5]. Decorating active sites onto the surface of nanoparticles can help modify and improve their function and, if designed appropriately, may aid in the CO_2 absorption process. For example, amine and oleic acid have been used to modify the surface of multi-walled carbon nanotubes and Fe_3O_4 nanoparticles, respectively, in water for the absorption of CO_2 and O_2 [25,26]. Nabipour et al. studied the effect of functionalized MWCNTs on CO_2 absorption [20]. It was found that the addition of 0.02 wt% carboxyl functionalized MWCNTs to Sulfinol-M led to 23.2% enhancement of the equilibrium solubility compared to based-solvent.

For CO_2 capture, different kinds of amine functional groups can be mixed to tailor the features of the nanofluid suspension, such as the absorption kinetics or loading capacity. Irani et al. compared the CO_2 absorption performance of methyl diethanolamine (MDEA) solution with/without amine-modified, reduced graphene oxide nanoparticles [27]. The CO_2 absorption capacity was promoted by 16.2% after nanoparticle addition. Moreover, amine functionalized nanoparticles were dispersed in MDEA solution and showed excellent stability. In another study by Irani et al., the addition of 0.2 wt% of polyethyleneimine functionalized HKUST-1 to aqueous solution of 40 wt% increased the CO_2 absorption capacity to 16% compared to based-solvent [19]. Yao et al. fabricated a hybrid nanofluid composed of a composite core of silica and poly(2-dimethylamino ethyl methacrylate) microgel and a shell of polyetheramine [28]. They used the prepared nanofluid for CO_2 absorption and obtained excellent absorption capacity.

In the case of water-base absorbing fluid, the hydrophilicity of the nanoparticles can enhance their water dispersibility, as well as accelerate the collision with CO_2 bubbles and crack the bubbles more easily increasing the mass transfer and, consequently, the convective motion of the nanofluid, leading to enhanced CO_2 capturing. Therefore, the effect of nanoparticles modified with functional active sites on CO_2 absorption from water-based fluids could be an important subject for the development of future CO_2 capture technologies. Moreover, amine-based solid sorbents in the form of dispersed nanoparticles have a significant potential of energy savings over amine solvents because they do not need the large amount of energy that must be consumed for heating and cooling operations to regenerate the liquid solvent solutions [18,29]. An additional advantage of this system is its suitability for pre-combustion processes which usually work at high pressures [10].

In this work, we modified the surface of Fe_3O_4 nanoparticles with different kinds of inorganic and organic reagents in order to prepare a symmetric, amine-based, nanodendritic absorbent and then studied their CO_2 absorption in a water-based nanofluid. Indeed, fabricating symmetric amine active sites at the end of the stabilized organic dendritic branches increases the polarity and uptake ability of the adsorbent via an acid-basic interaction and feeble chemical bond creation between the amine functional sites and CO_2 . Bis(phthaloyl)diethyleneetriamine was added to the modified Fe_3O_4 nanoparticles to make sure that symmetric amine sites were created at the ends of the nanodendritic adsorbent. To the best of our knowledge, this is the first report of a symmetric nanodendritic adsorbent for enhanced CO_2 absorption in water-based nanofluids. The effect of modification processes on the



Scheme 1. Schematic illustration of the synthesis of the modified nanoparticles.

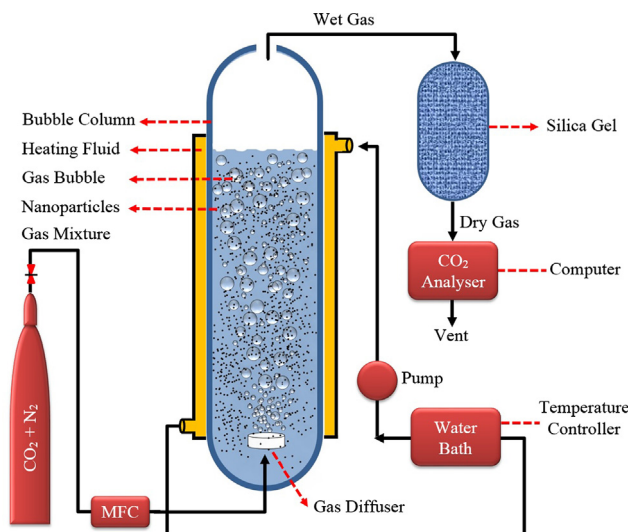
hydrophilicity and aggregation of the nanoparticles were studied and the effect of temperature, amount of nanofluid, and the absorption cycle on the best absorbent was investigated.

2. Experimental

2.1. Materials and characterization

All materials and solvents were purchased from Sigma-Aldrich. 0.1 M HCl/NaOH solutions and a pH meter (Metrohm pH-meter, model 691) was used to adjust the pH of the aqueous solutions. A Bruker

AV300 spectrometer in D₂O-d2 with tetramethylsilane was used as an internal standard to record the ¹H NMR and ¹³C NMR spectra. Melting points of prepared organic reagents were determined using an X-6 micro-melting point instrument. Fourier transform infrared (FTIR) spectra were obtained from 4000 to 500 cm⁻¹ on a Shimadzu FTIR Model-IRAffinity-1S (MIRacle 10), in which 64 scans were taken at a resolution of 2 cm⁻¹. Elemental analysis was conducted with a CHNO-Rapid Heraeus device (Wellesley, MA). Scanning (SEM) and transmission electron microscopy (TEM) images were taken using a Zeiss Gemini 500 SEM and a FEI T12 Spirit TEM STEM operated at 120 kV, respectively. X-ray photoelectron spectroscopy (XPS) was conducted



Scheme 2. Schematic of the CO_2 absorption experimental apparatus.

with a Surface Science device SSX-100 operated at a pressure of $\sim 2 \times 10^{-9}$ Torr and Al $\text{K}\alpha$ monochromatic X-rays (1486.6 eV) with 1 mm diameter beam size and a 55° emission angle. A hemispherical tester ascertained the electron kinetic energy by applying 50 V for high-resolution scans and a pass energy of 150 V for wide/survey scans.

2.2. Preparation of Fe_3O_4 nanoparticles

Fe_3O_4 nanoparticles (NPs) were synthesized using ferric and ferrous salt precursor materials. The water solvent of the reaction (150 mL) was degassed using N_2 gas flow through the preparation process [30]. In brief, 0.4 M FeCl_2 and 0.8 M FeCl_3 were added to 20 mL water under vigorous mechanical stirring for 25 min at 80 °C. Subsequently, we added 8 mL of NH_4OH , dropwise, to the solution and stirred for 30 min. The color of the homogeneous, brown solution turned to black, which confirmed the preparation of Fe_3O_4 nanoparticles. The black precipitate was separated and collected from the solution by utilizing an external magnetic field. After washing the powder with water and ethanol, the obtained Fe_3O_4 NPs were dispersed in ethanol and stored in a dark and 4 °C.

2.3. Synthesis of core-shell $\text{Fe}_3\text{O}_4@\text{SiO}_2$ NPs

The Fe_3O_4 NPs were dispersed in 150 mL water by an ultrasonic water bath, then 4.5 mL of aqueous ammonia (25 wt%) and 150 mL of ethanol were added to the solution under mechanical stirring [31]. Then, 1.1 mL of TEOS was added, dropwise, into this solution at 25 °C and stirred for 5 h. The resulting nanoparticles were collected using an external magnet and washed with water, ethanol, and acetone. The final core-shell NPs were dried at 70 °C in a vacuum oven for 12 h.

2.4. Synthesis of $\text{Fe}_3\text{O}_4@\text{SiO}_2\text{-NH}_2$

The propyl amine functionalized Fe_3O_4 nanoparticles were synthesized by refluxing 2.5 g of $\text{Fe}_3\text{O}_4@\text{SiO}_2$ with 5 mL 3-aminopropyl-trimethoxy silane (APTMS) in toluene (100 mL) for 24 h. The product was separated with an external magnet and washed with toluene, ethanol, and acetone, and then dried at 70 °C in a vacuum oven for 12 h. Hereafter, the APTES-modified $\text{Fe}_3\text{O}_4@\text{SiO}_2$ is identified as $\text{Fe}_3\text{O}_4@\text{SiO}_2\text{-NH}_2$.

2.5. Synthesis of $\text{Fe}_3\text{O}_4@\text{SiO}_2\text{-SNH}_2$

5 g of $\text{Fe}_3\text{O}_4@\text{SiO}_2\text{-NH}_2$ was dispersed in 100 mL of methanol and

2.5 mL of methyl acrylate and refluxed for 24 h. The obtained product was washed with methanol and acetone ($\text{Fe}_3\text{O}_4@\text{SiO}_2\text{-NMA}$). In the next step, 2 g of $\text{Fe}_3\text{O}_4@\text{SiO}_2\text{-NMA}$ was refluxed for 24 h with 1 g bis (phthaloyl)diethylenetriamine (BPA; synthesized based on the literature [32], see Supplementary data) in dimethyl formamide, and the resulting nanoparticles ($\text{Fe}_3\text{O}_4@\text{SiO}_2\text{-NBPA}$) were washed with acetone and dried at 70 °C in a vacuum oven for 5 h. The BPA was added to synthesize the symmetric amine sites at the ends of the carbon backbone of the dendritic branches. Symmetric amine sites were obtained by deprotecting the symmetric amines using hydrazine hydrate (N_2H_4) in acetonitrile and refluxed for a reaction time of 48 h. The resultant $\text{Fe}_3\text{O}_4@\text{SiO}_2\text{-SNH}_2$ was separated with an external magnet and washed with methanol, ethanol, and acetone sequentially, then dried in a vacuum oven (Scheme 1). The prepared $\text{Fe}_3\text{O}_4@\text{SiO}_2\text{-SNH}_2$ were stored in a dark and dry place.

2.6. Preparation of the nanofluids

Absorption measurements of CO_2 were done with distilled water and nanofluids. The nanofluids were prepared by dispersing 0.2 wt% nanoparticles (unless otherwise specified) in distilled water without the use of any surfactant and using a probe type ultrasonic agitator at 200 W for 15 min.

2.7. Experimental setup of CO_2 absorption

The CO_2 absorption experiment was performed in a home-built bubble column at atmospheric pressure. The column was made of a Plexiglas cylinder with an inner diameter of 2.5 cm and length of 50 cm. In all experiments, the absorption column was filled with 150 mL of the absorbent (nanofluid or distilled water). In order to keep the absorbent temperature constant, the column was covered by another Plexiglas cylinder where water was circulated. The temperature of the water jacket was controlled by a temperature controller. A schematic diagram of the experimental setup is shown in Scheme 2.

CO_2 , with a concentration of 8850 ppm (balanced with N_2), was supplied from a gas cylinder. The volumetric flow rate of the gas was fixed at 100 mL/min using a mass flow controller (MFC). The CO_2 containing gas mixture entered the column as small bubbles using a gas diffuser (4–10 μm pores) mounted at the bottom of the column. The bubbles contact the liquid phase and rise to the top. The unabsorbed gas flowed out the column and entered a silica gel column to remove the water vapor. Afterward, the CO_2 concentration in the exit gas stream was measured every 3 s over a period of 1800 s using a Testo 535 CO_2 analyzer.

We used Eq. (1) to calculate the amount of CO_2 absorbed, in which V_{CO_2} is the total volume of CO_2 absorbed, Q is the flowrate of the gas mixture entering the column, C_t is the concentration of CO_2 in the outgoing gas stream at time t , and C_{max} is the concentration of CO_2 in the gas cylinder.

$$V_{\text{CO}_2} = \sum_{t=0}^{t=1800} Q \times \left(C_{\text{max}} - \frac{C_t + C_{t+3}}{2} \right) \times 3 \quad (1)$$

The Enhancement Percentage (Eq. (2)) and Effective Absorption Ratio (Eq. (3)) explain the absorption improvement by nanofluid compared to base fluid. Indeed, these parameters are used to investigate the effects of nanoparticles on CO_2 absorption. The enhancement percentage is defined as the difference in the volume of CO_2 absorbed by the nanofluid and the base fluid divided by the volume absorbed by the base fluid, multiple by 100. The Effective Absorption ratio is defined as the volume of CO_2 absorbed by the nanofluid divided by the volume absorbed by the base fluid.

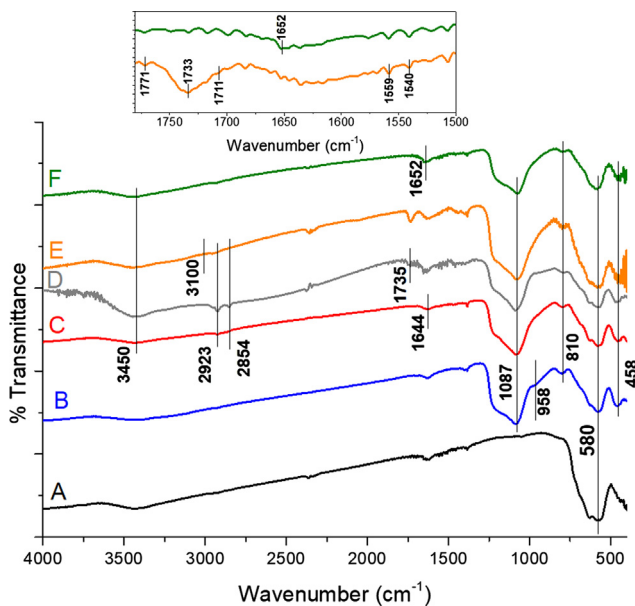


Fig. 1. FTIR spectra of (A) Fe_3O_4 , (B) $\text{Fe}_3\text{O}_4@\text{SiO}_2$, (C) $\text{Fe}_3\text{O}_4@\text{SiO}_2\text{-NH}_2$, (D) $\text{Fe}_3\text{O}_4@\text{SiO}_2\text{-NMA}$ (E) $\text{Fe}_3\text{O}_4@\text{SiO}_2\text{-NBPA}$, and (F) $\text{Fe}_3\text{O}_4@\text{SiO}_2\text{-SNH}_2$. The magnified FTIR spectra are provided in the supplementary data.

$$\text{Enhancement}(\%) = \frac{V_{\text{Absorbed CO}_2 \text{ by nanofluid}} - V_{\text{Absorbed CO}_2 \text{ by water}}}{V_{\text{Absorbed CO}_2 \text{ by water}}} \times 100 \quad (2)$$

$$\text{Effective absorbance ratio}(E) = \frac{V_{\text{Absorbed CO}_2 \text{ by nanofluid}}}{V_{\text{Absorbed CO}_2 \text{ by water}}} \quad (3)$$

3. Results and discussion

3.1. Characterization of the nanomaterials

We used FTIR to investigate the chemical structures of the prepared nanoparticles (Fe_3O_4) and as well as after they had been modified with various reagents (Fig. 1 and Fig. S1–S6). The Fe_3O_4 nanoparticles showed a strong absorption peak at 580 cm^{-1} , which we assigned to the stretching vibration of $\text{Fe}-\text{O}$ [33]. This peak was also visible in the other modified Fe_3O_4 materials (Fig. 1). For $\text{Fe}_3\text{O}_4@\text{SiO}_2$ nanoparticles, four new bands at 1087 and 958 , 810 and 458 cm^{-1} appeared, which correspond to the asymmetric stretching vibration of $\text{Si}-\text{O}-\text{Si}$, stretching vibration of the silica shell $\text{Si}-\text{OH}$, symmetric stretching vibrations of $\text{Si}-\text{O}-\text{Si}$, and the $\text{Fe}-\text{O}-\text{Si}$ stretching vibration, respectively [34]. These results confirmed the encapsulation of the Fe_3O_4 core by the silica shell. Decorating the surface of the $\text{Fe}_3\text{O}_4@\text{SiO}_2$ with APTES showed two new bands at 2923 and 2854 cm^{-1} related to the stretching vibration of the alkyl group of APTES [32,35,36]. However, the stretching vibration of $\text{Si}-\text{OH}$ at 958 cm^{-1} disappeared after the APTES treatment, which confirmed the successful preparation of $\text{Fe}_3\text{O}_4@\text{SiO}_2\text{-NH}_2$ [31,37] (Fig. 1). The observation of the $-\text{C}=\text{O}$ of the ester group at 1735 cm^{-1} implied that the amine groups of $\text{Fe}_3\text{O}_4@\text{SiO}_2\text{-NH}_2$ were subsequently converted to amide groups by the addition of methyl acrylate to produce $\text{Fe}_3\text{O}_4@\text{SiO}_2\text{-NMA}$, which was further modified with BPA to eventually be converted to a high density of symmetric amine groups (Fig. 1) [38]. In the next step of the synthesis, the phthaloyl protecting groups of the symmetric amines were detached using hydrazine after a reaction time of 48 h to prepare $\text{Fe}_3\text{O}_4@\text{SiO}_2\text{-NMBPA}$ (Fig. 1). The peaks intensity related the phthaloyl groups at 3100 , 1733 , and 1715 cm^{-1} were declined and removed after the treatment, which confirmed the successful deprotection of the symmetric amine groups and preparation of the dendritic amine group on

Table 1
Chemical composition of the synthesized nanoparticles.

Nanoparticle	Elemental analyses (wt%) ^a		Reactive functional site (mmol/g) ^b
	C	N	
Fe_3O_4 ^a	0.83	–	–
$\text{Fe}_3\text{O}_4@\text{SiO}_2$	1.34	–	–
$\text{Fe}_3\text{O}_4@\text{SiO}_2\text{-NH}_2$	4.36	1.54	1.10
$\text{Fe}_3\text{O}_4@\text{SiO}_2\text{-SNH}_2$	7.76	2.84	2.02

^a Nitrogen and carbon was obtained from the elemental analysis.

^b Determined from the N-contents.

the surface of the $\text{Fe}_3\text{O}_4@\text{SiO}_2\text{-SNH}_2$ while the new peak related to the amine sites at 1652 cm^{-1} was appeared [39,40]. The CHN elemental analysis results showed that, by modifying the surface of the Fe_3O_4 with APTES and diethylenetriamine, the concentration of N increased from 1.10 to 2.02 mmol/g (Table 1), which also confirmed the successful preparation of the nanodendritic absorbent (Fig. 1).

Fig. 2 shows the TEM and SEM images of the as-prepared Fe_3O_4 and $\text{Fe}_3\text{O}_4@\text{SiO}_2\text{-SNH}_2$ structures. The TEM image of the Fe_3O_4 nanoparticles indicated the fine, spherical structure and the TEM of the modified Fe_3O_4 with silica shell and dendritic group ($\text{Fe}_3\text{O}_4@\text{SiO}_2\text{-SNH}_2$) resulted in a Fe_3O_4 core of $\sim 50\text{ nm}$ in diameter and a shell of $\sim 4.3\text{--}5\text{ nm}$ in thickness. The low-magnification SEM image of $\text{Fe}_3\text{O}_4@\text{SiO}_2\text{-SNH}_2$ showed the spherical nano-framework with a diameter less than 50 nm , and the magnified SEM images revealed the uneven spherical surface of the modified substrate, which confirmed the successful surface modification of the magnetic support.

The thermal stability of the Fe_3O_4 , $\text{Fe}_3\text{O}_4@\text{SiO}_2\text{-NH}_2$ and $\text{Fe}_3\text{O}_4@\text{SiO}_2\text{-SNH}_2$ were recorded using thermos-gravimetric analysis TGA under N_2 from $30\text{ }^\circ\text{C}$ up to $650\text{ }^\circ\text{C}$ with the heating rate of $4\text{ }^\circ\text{C}/\text{min}$ (Fig. 3). The pristine Fe_3O_4 nanoparticle, without any protecting agent, showed 1.2% weight loss between 30 and $400\text{ }^\circ\text{C}$ which could have resulted from the evaporation of adsorbed water. The samples of $\text{Fe}_3\text{O}_4@\text{SiO}_2\text{-NH}_2$ and $\text{Fe}_3\text{O}_4@\text{SiO}_2\text{-SNH}_2$ showed 3.7 and 3.2% weight loss, respectively, after $650\text{ }^\circ\text{C}$. In fact, with increasing the temperature from 30 to $100\text{ }^\circ\text{C}$ the adsorbed water molecules are evaporated and, when the temperature is raised further to $650\text{ }^\circ\text{C}$, more weight loss occurred [41]. At higher temperatures, most of the oxidation, degradation and decomposition processes are carried out. However, the low weight loss of $\text{Fe}_3\text{O}_4@\text{SiO}_2\text{-SNH}_2$ (3.2%) after $650\text{ }^\circ\text{C}$ could be attributed to the high tendency of the dendritic group, and its active sites, to make a coordination ligand with metallic cations and be retained on the surface. This would eventually suppress their detachment and degradation at high temperature [41–43].

We used XPS to analyze the chemical composition and functional sites of the prepared adsorbents. The wide-scan XPS spectra for the Fe_3O_4 , $\text{Fe}_3\text{O}_4@\text{SiO}_2$, $\text{Fe}_3\text{O}_4@\text{SiO}_2\text{-NH}_2$, $\text{Fe}_3\text{O}_4@\text{SiO}_2\text{-NMA}$, and $\text{Fe}_3\text{O}_4@\text{SiO}_2\text{-SNH}_2$ samples are illustrated in Fig. 4A. The Fe_3O_4 nanoparticles feature two peaks at 710.5 and 725.1 eV , attributed to $\text{Fe }2\text{p}_{3/2}$ and $\text{Fe }2\text{p}_{1/2}$, respectively (Fig. 4B). The appearance of $\text{Si }2\text{s}$ and $\text{Si }2\text{p}$ peaks for $\text{Fe}_3\text{O}_4@\text{SiO}_2$ confirmed the generation of the SiO_2 shell on the surface of the Fe_3O_4 ; however, the Fe_3O_4 peaks were still observed, which implies that the thickness of the SiO_2 shell is below 10 nm [44–46], as was observed in TEM imaging. The intensity of the Si element on $\text{Fe}_3\text{O}_4@\text{SiO}_2\text{-NH}_2$ increased in comparison to the $\text{Fe}_3\text{O}_4@\text{SiO}_2$ (Fig. 4A) and also a new peak corresponding to $\text{N }1\text{s}$ appeared at 408.5 eV (Fig. 4C). This suggests the immobilization of APTES on the surface of the $\text{Fe}_3\text{O}_4@\text{SiO}_2\text{-NH}_2$ [47]. For the $\text{Fe}_3\text{O}_4@\text{SiO}_2\text{-NMA}$ and $\text{Fe}_3\text{O}_4@\text{SiO}_2\text{-SNH}_2$ samples, the intensity of the Si peak decreased, which could be related to the successful fabrication and addition of more organic groups, such as methyl acrylate and symmetric amine groups on the surface of Fe_3O_4 [48]. Furthermore, the position and shape of the $\text{N }1\text{s}$ peak changed after adding methyl acrylate and symmetric

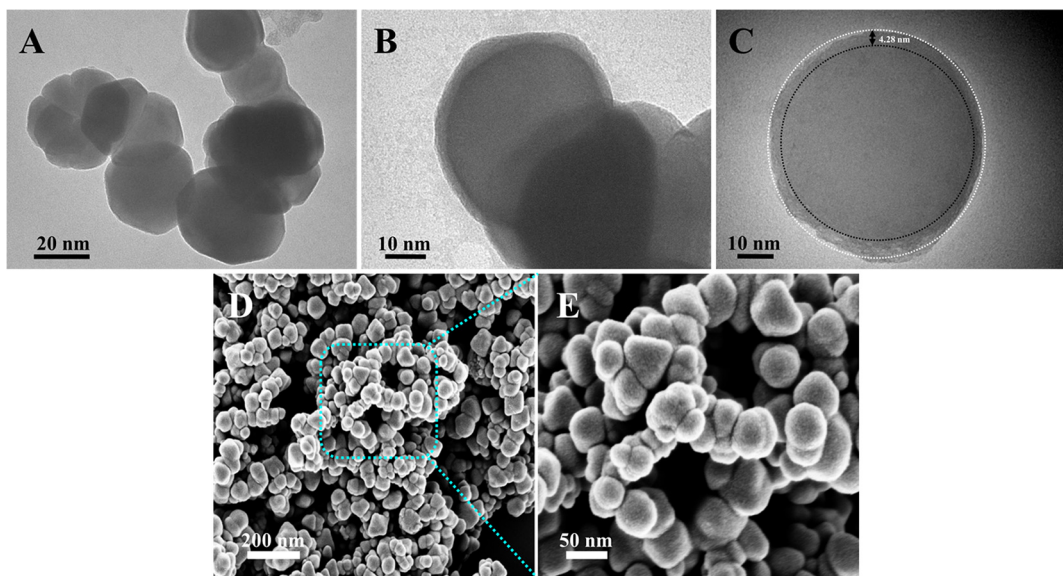


Fig. 2. TEM images of (A) Fe_3O_4 , (B and C) $\text{Fe}_3\text{O}_4@\text{SiO}_2\text{-SNH}_2$, and (D and E) SEM images of $\text{Fe}_3\text{O}_4@\text{SiO}_2\text{-SNH}_2$.

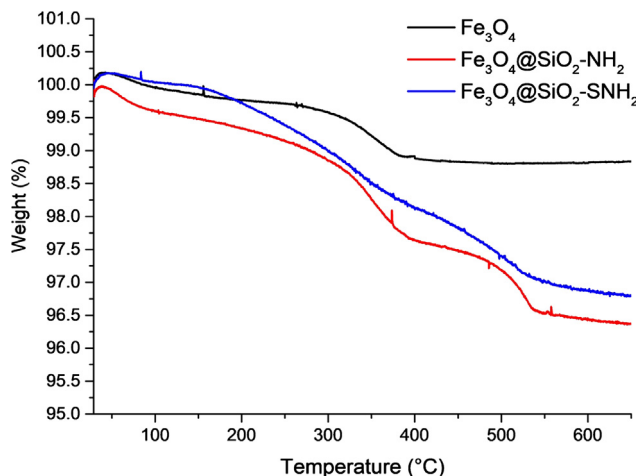


Fig. 3. TGA thermogram of the prepared nanoparticles.

diethylenetriamine groups from 408.5 eV to 405.9 and 407.2 eV for $\text{Fe}_3\text{O}_4@\text{SiO}_2\text{-NMA}$ (Fig. 4D) and $\text{Fe}_3\text{O}_4@\text{SiO}_2\text{-SNH}_2$ (Fig. 4E), respectively. That again confirms the preparation of symmetric amines on the surface of $\text{Fe}_3\text{O}_4@\text{SiO}_2\text{-SNH}_2$ as it was shown in the FTIR results.

3.2. CO_2 absorption in pure water and the nanofluids

Fig. 5A and B show the absorption efficiency and rates of CO_2 capture as a function of time by water and the five nanofluids of Fe_3O_4 , $\text{Fe}_3\text{O}_4@\text{SiO}_2$, $\text{Fe}_3\text{O}_4@\text{SiO}_2\text{-NH}_2$, $\text{Fe}_3\text{O}_4@\text{SiO}_2\text{-NMA}$, and $\text{Fe}_3\text{O}_4@\text{SiO}_2\text{-SNH}_2$. The nanofluids of the Fe_3O_4 , $\text{Fe}_3\text{O}_4@\text{SiO}_2$, $\text{Fe}_3\text{O}_4@\text{SiO}_2\text{-NH}_2$, and $\text{Fe}_3\text{O}_4@\text{SiO}_2\text{-SNH}_2$ were used to study their absorption capacity towards CO_2 in comparison with pure water. The temperature and adsorbent amount were kept constant at 30 °C and 0.2 wt% during all experiments, respectively.

Adding Fe_3O_4 nanoparticles to the water considerably raised the absorption capacity of the fluid system towards CO_2 (22.4%); however, when the surface of the Fe_3O_4 was modified with TEOS, the $\text{Fe}_3\text{O}_4@\text{SiO}_2$ nanofluid absorbed less CO_2 (8.32%) in comparison with the as-prepared Fe_3O_4 . However, $\text{Fe}_3\text{O}_4@\text{SiO}_2$ /water nanofluid was still better than the absorption efficiency of the pure water fluid. Fe_3O_4 nanoparticles are hydrophilic, demonstrating a water contact angle of 0°, but, when modified with TEOS, the surface hydrophilicity of the Fe_3O_4

core decreased so that the water contact angle of $\text{Fe}_3\text{O}_4@\text{SiO}_2$ was 55° (Fig. 5C). This implied that $\text{Fe}_3\text{O}_4@\text{SiO}_2$ has lower hydrophilicity in comparison with Fe_3O_4 which can cause the aggregation and agglomeration of the $\text{Fe}_3\text{O}_4@\text{SiO}_2$ nanofluid and, consequently, lead to the decreased velocity disturbance field, motion of the nanoparticles, and mass transfer surface of the $\text{Fe}_3\text{O}_4@\text{SiO}_2$ [31,47,49]. Furthermore, the smaller size of the Fe_3O_4 in comparison with $\text{Fe}_3\text{O}_4@\text{SiO}_2$ increased the mass transfer and dispersion of the Fe_3O_4 in the nanofluid, which explains its, approximately, three-fold CO_2 absorption rate when compared to $\text{Fe}_3\text{O}_4@\text{SiO}_2$ (Fig. 5D) [5,50]. Furthermore, the absorption of CO_2 on the surface of Fe_3O_4 and $\text{Fe}_3\text{O}_4@\text{SiO}_2$ could be performed through physical interaction due to the lack of amine functional sites. However, we observed that the $\text{Fe}_3\text{O}_4@\text{SiO}_2\text{-NH}_2$ and $\text{Fe}_3\text{O}_4@\text{SiO}_2\text{-SNH}_2$ nanofluids obtained a significant enhancement in CO_2 absorption compared to the other nanofluids. In Fig. 5B and D, the real-time capture capacity of the $\text{Fe}_3\text{O}_4@\text{SiO}_2\text{-SNH}_2$ nanofluid in the initial period (within 90 sec) was larger than the $\text{Fe}_3\text{O}_4@\text{SiO}_2\text{-NH}_2$ sample, which indicates that the nanoparticles could markedly enhance the CO_2 absorption rate in the diffusion-controlled phase. $\text{Fe}_3\text{O}_4@\text{SiO}_2\text{-SNH}_2$ features the highest density of the nucleophilic active sites and a better chemical interaction with CO_2 , exhibited by the higher gas absorption of 49.7%, through the intact process, with respect to the host water fluid, while $\text{Fe}_3\text{O}_4@\text{SiO}_2\text{-NH}_2$ showed 47.1% CO_2 absorption (Fig. 5D). Considering the nanoparticles used throughout the entire process of CO_2 absorption (1800 s) in nanofluid system, these can significantly raise the CO_2 absorption rate and capacity in comparison with the water base fluid.

Although both amine bearing absorbents are decorated with primary amine groups and both are hydrophilic (Fig. 5C), they are not the same amine molecules and structures, and thus this variation in the CO_2 absorption may correspond to the lower capture capacity of $\text{Fe}_3\text{O}_4@\text{SiO}_2\text{-NH}_2$ [51]. The immobilized dendritic amine groups on the surface of the $\text{Fe}_3\text{O}_4@\text{SiO}_2\text{-SNH}_2$ are symmetric and the branches of the dendritic amine groups could be easily dispersed in water due to the longer distance from the core of the $\text{Fe}_3\text{O}_4@\text{SiO}_2$ than $\text{Fe}_3\text{O}_4@\text{SiO}_2\text{-NH}_2$. Based on these findings, we chose $\text{Fe}_3\text{O}_4@\text{SiO}_2\text{-SNH}_2$ for further study.

3.3. CO_2 capture capacity of $\text{Fe}_3\text{O}_4@\text{SiO}_2\text{-SNH}_2$ at different solution temperatures

Fig. 6A shows the absorption efficiency of CO_2 by $\text{Fe}_3\text{O}_4@\text{SiO}_2\text{-SNH}_2$ at different temperatures ranging from 298 to 313 K and the

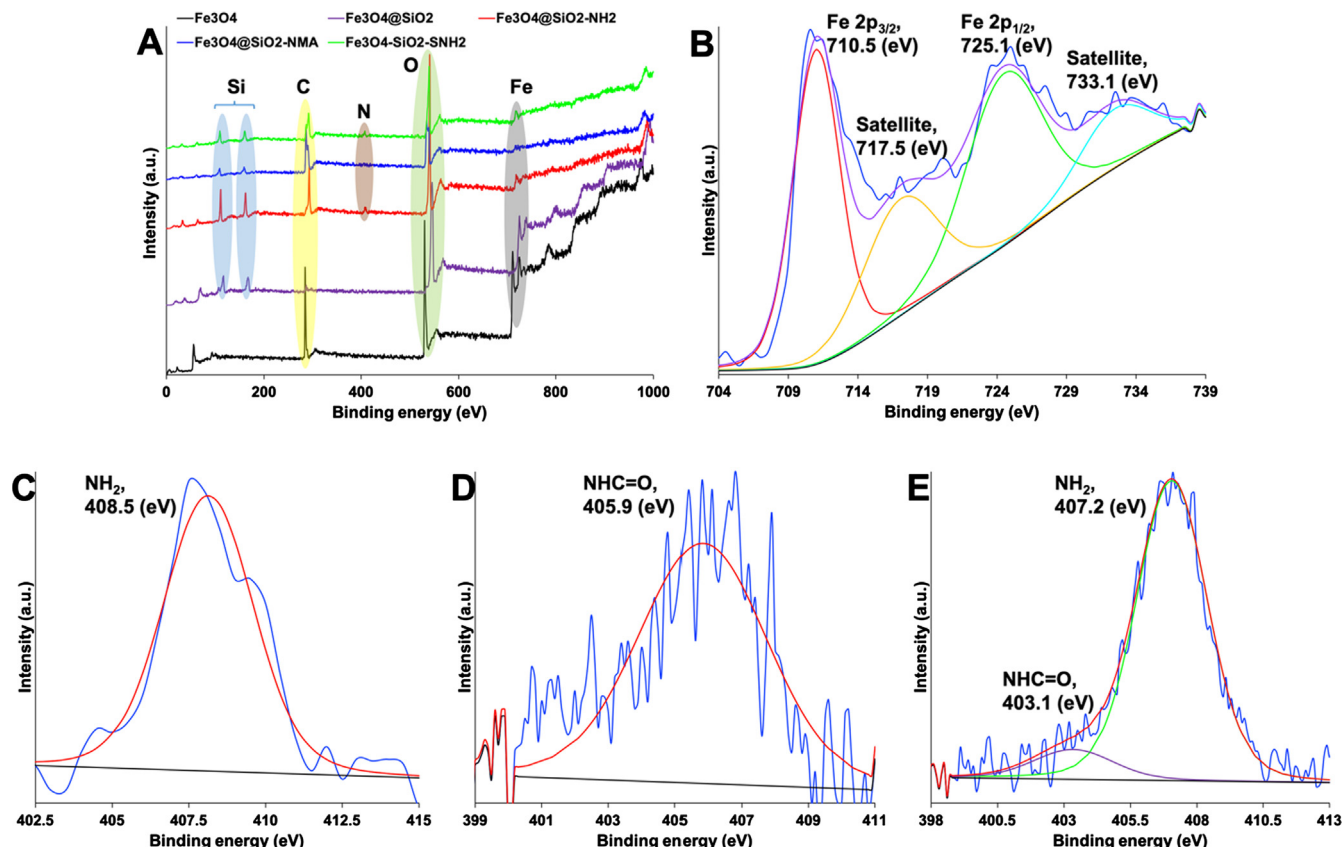


Fig. 4. (A) XPS survey spectrum of Fe_3O_4 , $\text{Fe}_3\text{O}_4@\text{SiO}_2$, $\text{Fe}_3\text{O}_4@\text{SiO}_2\text{-NH}_2$, $\text{Fe}_3\text{O}_4@\text{SiO}_2\text{-NMA}$, and $\text{Fe}_3\text{O}_4@\text{SiO}_2\text{-SNH}_2$. (B) Fe 2p high-resolution spectrum of Fe_3O_4 , and N 1s high resolution spectra of (C) $\text{Fe}_3\text{O}_4@\text{SiO}_2\text{-NH}_2$, (D) $\text{Fe}_3\text{O}_4@\text{SiO}_2\text{-NMA}$, and (E) $\text{Fe}_3\text{O}_4@\text{SiO}_2\text{-SNH}_2$.

adsorbent amount of 0.2 wt%. We observed that CO_2 capture with increasing temperature decreased from 53.1 to 35.1%, respectively, at an initial CO_2 concentration of 8850 ppm. The obtained maximum absorption capacity of CO_2 at 298 K implies the proper and positive interaction and capturing of CO_2 through $\text{Fe}_3\text{O}_4@\text{SiO}_2\text{-SNH}_2$ from aqueous solution in mild condition; however, desorption of the adsorbed CO_2 and regeneration of the active sites of $\text{Fe}_3\text{O}_4@\text{SiO}_2\text{-SNH}_2$ could be performed through the low energy consumption process [51,52]. In fact, by enhancing the solution temperature, the activation energy of the nanoparticle system increases and, therefore, the nanodendritic adsorbent within the fluid gains more mobility and active motion. Consequently, the dynamic motion created from the elevated temperature and activation energy causes more interactions and collisions between the nano-sized adsorbents, which results in the decreasing CO_2 capture capacity of $\text{Fe}_3\text{O}_4@\text{SiO}_2\text{-SNH}_2$ in addition to the accelerating desorption of the dissolved CO_2 on the adsorbent [2,18].

3.4. The effect of nanofluid dosage

We also studied the effect of the quantity of adsorbent (0.1–0.5 wt %) on the capture of 8850 ppm CO_2 at $25 \pm 2^\circ\text{C}$ (Fig. 6B). The results implied that CO_2 capture increased as the adsorbent dosage increased, therefore the density and concentration of the CO_2 attracting active sites enhanced. Surprisingly, the capture efficiency of CO_2 increased more than two-fold from 32.1 to 70.3% as the amount of $\text{Fe}_3\text{O}_4@\text{SiO}_2\text{-SNH}_2$ adsorbent was increased from 0.1 to 0.4 wt%, respectively. However, by increasing the amount of adsorbent to 0.5 wt%, the capture capacity of $\text{Fe}_3\text{O}_4@\text{SiO}_2\text{-SNH}_2$ decreased to 68%. In fact, in lower concentrations of the adsorbent, dispersion of the adsorbent in aqueous solution takes place easily and there is no outcome of the mass transfer decline because of the slight viscosity altering the reactive sites of the $\text{Fe}_3\text{O}_4@\text{SiO}_2\text{-SNH}_2$, which are more accessible to the CO_2 molecule

[18]. Furthermore, by increasing the nanoparticle concentration to 0.4 wt% in the vicinity of the bubble and the liquid interface in the nanofluid, the diffusion boundary layer of the bubbles is more quickly surrounded by the adsorbent and the thickness of the layer decreases. Therefore, the diffusion and mass transfer into the liquid film is enhanced through the hydrodynamic effect [2,53]. However, by increasing the adsorbent to 0.5 wt%, the chance of collisions and aggregation of nanodendritic materials increased, which creates a decline in the Brownian motion due to the inter-particle attraction, suppressing the adsorbent motion [54,55] and, thus, accelerating the blockage of the active sites and causing a reduction in the total surface area, as well as increasing the diffusion path length of CO_2 capture and a decreasing in the mass diffusion [50,56] (Scheme 3). In fact, the existence of too many nanoparticles in the base fluid hinders the interaction between the CO_2 and water which, consequently, decreases the absorption of CO_2 on $\text{Fe}_3\text{O}_4@\text{SiO}_2\text{-SNH}_2$ [57]. Based on these findings, we used 0.4 wt% of adsorbent as the optimal amount for the remaining trials.

3.5. Multiple cycles of CO_2 adsorption-desorption

We studied the reusability and reactivation of the nanodendritic's active sites for CO_2 by performing five cycles of CO_2 absorption in nanofluid system at 25 °C and 0.4 wt% of adsorbent. Before each run, the $\text{Fe}_3\text{O}_4@\text{SiO}_2\text{-SNH}_2$ was fully regenerated under N_2 gas flow after 12 h at 353 K. After five cycles of CO_2 adsorption-desorption, the $\text{Fe}_3\text{O}_4@\text{SiO}_2\text{-SNH}_2$ only lost 4% of its adsorption capacity (Fig. 6C) and all of the absorbed CO_2 molecules were desorbed and detected following the CO_2 desorption process, which implied that the $\text{Fe}_3\text{O}_4@\text{SiO}_2\text{-SNH}_2$ was able to retain, recover, and regenerate its full active sites and demonstrated stable efficiency throughout its repeated use and thermal treatment at 353 K.

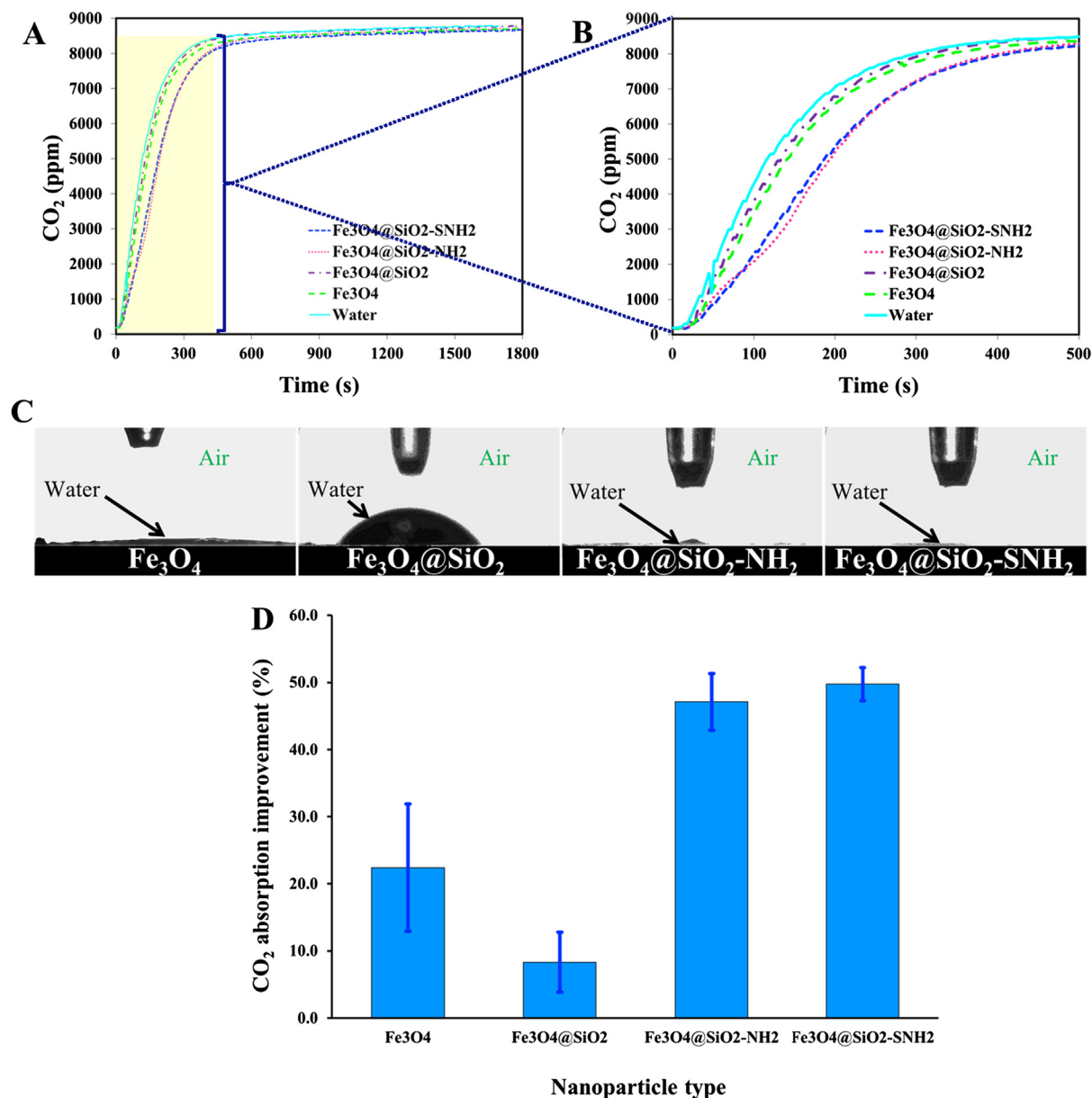


Fig. 5. (A and B) output CO₂ concentration as a function of time at the temperature of 30°C and nanoparticle amount of 0.2 wt%, (C) water wettability of the prepared nanoparticles in air, and (D) % of CO₂ enhancement of various nanoparticles in water.

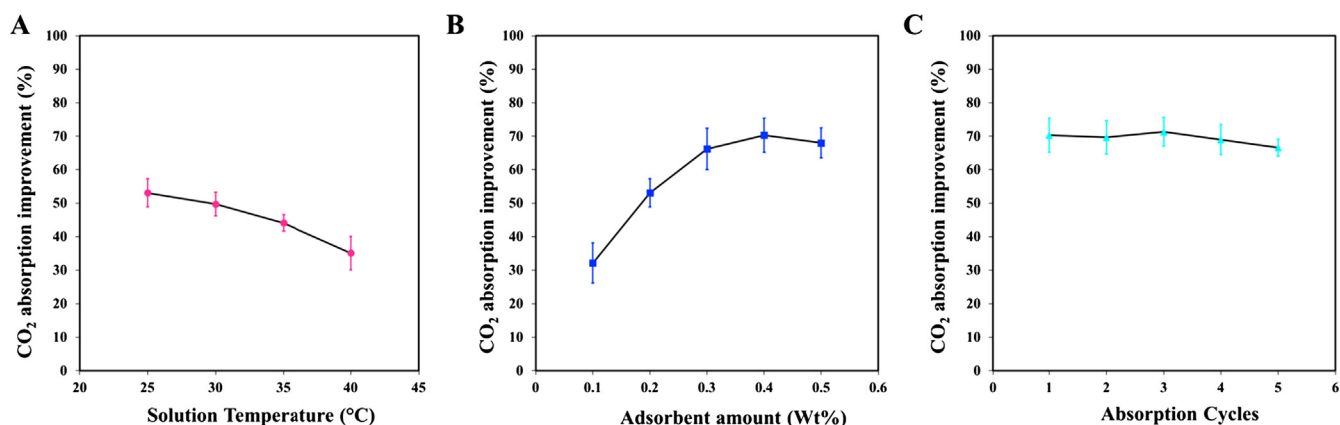
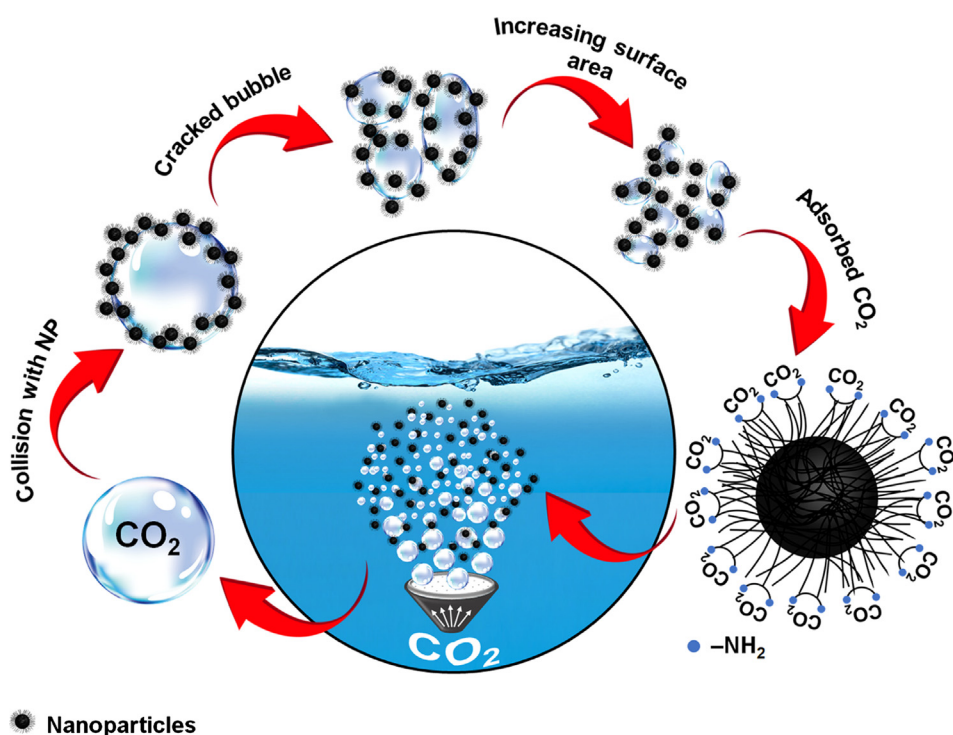


Fig. 6. CO₂ absorption improvement versus (A) solution temperature at 0.2 wt% of adsorbent, (B) adsorbent amount at 25 °C and (C) absorption cycles (at constant temperature and adsorbent amount of 25 °C and 0.4 wt%, respectively).



Scheme 3. Absorption mechanisms of bubble cracking by the nanoparticles and absorption of CO_2 on the active sites of the absorbent in the nanofluid system.

3.6. CO_2 absorption reaction mechanism

To understand the interaction of CO_2 with the reactive sites of the best nanofluidic systems, we investigated the FTIR spectra of the $\text{Fe}_3\text{O}_4@\text{SiO}_2\text{-NH}_2$ and $\text{Fe}_3\text{O}_4@\text{SiO}_2\text{-SNH}_2$ nanoparticles after CO_2 absorption (Fig. 7). $\text{Fe}_3\text{O}_4@\text{SiO}_2\text{-NH}_2@\text{CO}_2$ showed new peaks when compared to the pristine material, confirming the interaction and absorption of CO_2 on its surface. The appearance of these peaks at 1717, 1418, and 1358–1347 cm^{-1} may correspond to the CO_2 stretching vibration, carbonyl group of NCOOH , and the C–N stretching vibration of the NHCOO^- and NCOO^- skeleton, respectively [58]. Meanwhile, the FTIR spectrum of $\text{Fe}_3\text{O}_4@\text{SiO}_2\text{-SNH}_2@\text{CO}_2$ also resulted in additional features and changes related to $\text{Fe}_3\text{O}_4@\text{SiO}_2\text{-SNH}_2$, where peaks at 1514 and 1446 cm^{-1} could be attributed to the COO^- stretching vibration and C–N stretching vibration of NHCOO^- , respectively [59,60] (Fig. 7). Furthermore, the changes in the intensity of the FTIR spectra of

the $\text{Fe}_3\text{O}_4@\text{SiO}_2\text{-NH}_2$ and $\text{Fe}_3\text{O}_4@\text{SiO}_2\text{-SNH}_2$ before and after absorption of CO_2 at 2330–2400 cm^{-1} and 1600–1670 cm^{-1} (Figs. S7 and S8), respectively, could be related to the chemical interaction of the amine sites with the absorbed carbon dioxide as well [61]. In fact, the appearance of some stretching vibration peaks related to COO^- , NHCOO^- , and NCOOH could result from the interaction between the CO_2 and amine groups of the nanoparticle which obey anionic and cationic mechanisms. In the nanofluidic system, CO_2 , as an anionic component, interacts with the available and reactive amine groups, which are cationic, and generate an intermediate that eventually deprotonates the intermediates producing carbamate and protonated groups on the surface of the nanoparticles, as well as stabilized CO_2 on the solid surface as depicted in the following [62,63]:

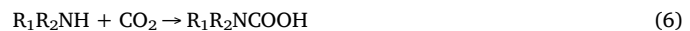
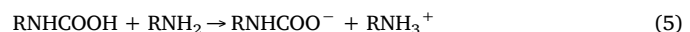


Table 2 shows the results of previous studies that used different nanofluids for improved CO_2 absorbance along with the results obtained in this work. Although an accurate comparison is difficult due to different absorbent characteristics, contactor type, and operating parameters, this study shows considerably greater improvement than previous works.

4. Conclusion

In this study, the absorption efficiency and rates of CO_2 capture as a function of time in water base nanofluid in the presence of five nanofluids of Fe_3O_4 , $\text{Fe}_3\text{O}_4@\text{SiO}_2$, $\text{Fe}_3\text{O}_4@\text{SiO}_2\text{-NH}_2$, $\text{Fe}_3\text{O}_4@\text{SiO}_2\text{-NMA}$ and $\text{Fe}_3\text{O}_4@\text{SiO}_2\text{-SNH}_2$ were studied. The reagents with various functional groups, as well as hydrophobic and hydrophilic characteristics, were chosen to evaluate their effect on the absorption of the CO_2 . It was observed that nodandritic absorbents with symmetric amine sites ($\text{Fe}_3\text{O}_4@\text{SiO}_2\text{-SNH}_2$) significantly enhanced (70%) CO_2 absorption over

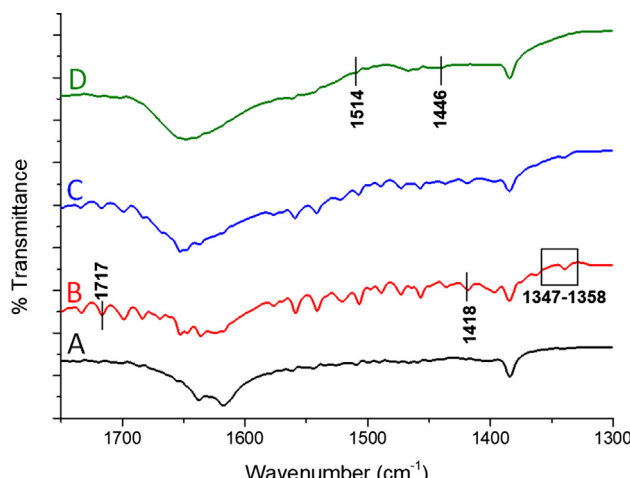


Fig. 7. FTIR spectra of the (A and B) $\text{Fe}_3\text{O}_4@\text{SiO}_2\text{-NH}_2$ and (C and D) $\text{Fe}_3\text{O}_4@\text{SiO}_2\text{-SNH}_2$ nanoparticles before and after CO_2 absorption, respectively.

Table 2Common use of nanofluids for CO₂ absorbance improvement.

E	% Enhancement	Base Fluid	Nanoparticle	T (°C)	Solid loading	Contactor type	Ref
1.7	70.3	Water	Fe ₃ O ₄ @SiO ₂ -SNH ₂	25	0.4 W%	Bubble column	This study
1.29	–	MDEA	TiO ₂	35	0.06 kg/m ³	Bubble column	[1]
1.13	–	MDEA	Al ₂ O ₃	35	0.08 kg/m ³	Bubble column	[1]
1.09	–	MEA	TiO ₂	35	0.08 kg/m ³	Bubble column	[1]
1.04	–	MEA	Al ₂ O ₃	35	0.06 kg/m ³	Bubble column	[1]
1.03	4.5	Methanol	Al ₂ O ₃	20	0.01 vol%	Bubble column	[50]
1.025	–	Methanol	SiO ₂	20	0.01 vol%	Bubble column	[50]
1.11	–	MDEA	TiO ₂	20	0.8 W%	Bubble column	[64]
–	24	Water	SiO ₂	25	0.021 W%	Bubble column	[65]
–	36	Water	FCNT ^a	17	4 vol%	Bubble column	[66]
–	8.3	Methanol	Al ₂ O ₃	10	0.01 vol%	Bubble column	[67]
1.2	–	18.8 W% NH ₃ /water	CNT	14	0.2 W%	Bubble column	[68]
–	12.5	NaCl solution	Al ₂ O ₃	20	0.01 vol%	Bubble column	[69]
–	33	DEA	Al ₂ O ₃	25	0.05 vol%	Wetted wall column	[70]
–	40	DEA	SiO ₂	25	0.05 vol%	Wetted wall column	[70]
–	9.4	Methanol	Al ₂ O ₃	22	0.05 vol%	Tray column	[71]
–	9.7	Methanol	SiO ₂	22	0.05 vol%	Tray column	[71]
–	21	Water	SiO ₂	35	0.1 W%	Batch vessel	[23]
–	18	Water	Al ₂ O ₃	35	0.1 W%	Batch vessel	[23]
–	24	Water	Fe ₃ O ₄	35	0.02 W%	Batch vessel	[23]
–	34	Water	CNT	35	0.02 W%	Batch vessel	[23]
–	23	MDEA	CNT	35	0.02 W%	Batch vessel	[23]
–	43.8	Water	Fe ₃ O ₄	30	0.15 W%	HFMC ^b	[72]
–	38	Water	CNT	30	0.1 W%	HFMC	[72]
–	25.9	Water	SiO ₂	30	0.05 W%	HFMC	[72]
–	3	Water	Al ₂ O ₃	30	0.05 W%	HFMC	[72]

^a Amine-functionalized multi-walled carbon nanotube.^b Hollow fiber membrane contactors.

the other nanofluids used, and also of the most reported nanoparticles in the literature. Fe₃O₄@SiO₂-SNH₂ retains its regeneration performance, even after 5 cycles, and lost only 4% of its absorption efficiency. Finally, Fe₃O₄@SiO₂-SNH₂, as a green, low-cost and regenerable absorbent, showed high CO₂ absorption through the water-based nanofluidic system, and could therefore be used as a highly promising absorbent of CO₂ in water.

Acknowledgments

This work made use of the Cornell Center for Materials Research's Shared Facilities, which are supported through the NSF MRSEC program (DMR-1719875).

Appendix A. Supplementary material

Supplementary data to this article can be found online at <https://doi.org/10.1016/j.apenergy.2019.03.105>.

References

- Jiang J, Zhao B, Zhuo Y, Wang S. Experimental study of CO₂ absorption in aqueous MEA and MDEA solutions enhanced by nanoparticles. *Int J Greenhouse Gas Control* 2014;29:135–41.
- Lee JW, Torres Pineda I, Lee JH, Kang YT. Combined CO₂ absorption/regeneration performance enhancement by using nanoabsorbents. *Appl Energy* 2016;178:164–76.
- Figueroa JD, Fout T, Plasynski S, McIlvried H, Srivastava RD. Advances in CO₂ capture technology—The U.S. Department of energy's carbon sequestration program. *Int J Greenhouse Gas Control* 2008;2:9–20.
- Azizi M, Mousavi SA. CO₂/H₂ separation using a highly permeable polyurethane membrane: molecular dynamics simulation. *J Mol Struct* 2015;1100:401–14.
- Zhang Z, Cai J, Chen F, Li H, Zhang W, Qi W. Progress in enhancement of CO₂ absorption by nanofluids: a mini review of mechanisms and current status. *Renew Energy* 2018;118:527–35.
- Said S, Govindaraj V, Herri J-M, Ouabas Y, Khodja M, Belloum M, et al. A study on the influence of nanofluids on gas hydrate formation kinetics and their potential: application to the CO₂ capture process. *J Nat Gas Sci Eng* 2016;32:95–108.
- Seddigh E, Azizi M, Sani ES, Mohebbi-Kalhori D. Investigation of poly(ether-b-amide)/nanosilica membranes for CO₂/CH₄ separation. *Chin J Polym Sci* 2014;32:402–10.
- Archane A, Fürst W, Provost E. Influence of Poly(ethylene oxide) 400 (PEG400) on the absorption of CO₂ in diethanolamine (DEA)/H₂O systems. *J Chem Eng Data* 2011;56:1852–6.
- Porcheron F, Jacquin M, El Hadri N, Saldana-Miranda D, Goulon A, Faraj A. Graph machine based-QSAR approach for modeling thermodynamic properties of amines: application to CO₂ capture in postcombustion. *Oil Gas Sci Technol – Revue d'IFP Energies nouvelles* 2013;68:449–86.
- Lee JW, Torres Pineda I, Lee JH, Kang YT. Combined CO₂ absorption/regeneration performance enhancement by using nanoabsorbents. *Appl Energy* 2016;178:164–76.
- Wang D, Li S, Liu F, Gao L, Sui J. Post combustion CO₂ capture in power plant using low temperature steam upgraded by double absorption heat transformer. *Appl Energy* 2018;227:603–12.
- Tobiesen FA, Haugen G, Hartono A. A systematic procedure for process energy evaluation for post combustion CO₂ capture: case study of two novel strong bi-carbonate-forming solvents. *Appl Energy* 2018;211:161–73.
- Oh S-Y, Yun S, Kim J-K. Process integration and design for maximizing energy efficiency of a coal-fired power plant integrated with amine-based CO₂ capture process. *Appl Energy* 2018;216:311–22.
- Ji L, Yu H, Li K, Yu B, Grigore M, Yang Q, et al. Integrated absorption-mineralisation for low-energy CO₂ capture and sequestration. *Appl Energy* 2018;225:356–66.
- Du Y, Wang Y, Rochelle GT. Piperazine/4-hydroxy-1-methylpiperidine for CO₂ capture. *Chem Eng J* 2017;307:258–63.
- Liu H, Gao H, Idem R, Tontiwachwuthikul P, Liang Z. Analysis of CO₂ solubility and absorption heat into 1-dimethylamino-2-propanol solution. *Chem Eng Sci* 2017;170:3–15.
- Liu H, Li M, Luo X, Liang Z, Idem R, Tontiwachwuthikul P. Investigation mechanism of DEA as an activator on aqueous MEA solution for postcombustion CO₂ capture. *AIChE J* 2018;64:2515–25.
- Lee JS, Lee JW, Kang YT. CO₂ absorption/regeneration enhancement in DI water with suspended nanoparticles for energy conversion application. *Appl Energy* 2015;143:119–29.
- Irani V, Tavasoli A, Maleki A, Vahidi M. Polyethyleneimine-functionalized HKUST-1/MDEA nanofluid to enhance the absorption of CO₂ in gas sweetening process. *Int J Hydrogen Energy* 2018;43:5610–9.
- Nabipour M, Keshavarz P, Raeissi S. Experimental investigation on CO₂ absorption in Sulfonol-M based Fe 3 O 4 and MWCNT nanofluids. *Int J Refrig* 2017;73:1–10.
- Pineda IT, Choi CK, Kang YT. CO₂ gas absorption by CH₃OH based nanofluids in an annular contactor at low rotational speeds. *Int J Greenhouse Gas Control* 2014;23:105–12.
- Choi SUS, Eastman JA. Enhancing thermal conductivity of fluids with nanoparticles. IL (United States): Argonne National Lab; 1995.
- Rahmatmand B, Keshavarz P, Ayatollahi S. Study of absorption enhancement of CO₂ by SiO₂, Al₂O₃, CNT, and Fe₃O₄ nanoparticles in water and amine solutions. *J Chem Eng Data* 2016;61:1378–87.
- Saidur R, Leong KY, Mohammad HA. A review on applications and challenges of nanofluids. *Renew Sustain Energy Rev* 2011;15:1646–68.
- Jorge L, Coulombe S, Girard-Lauriault P-L. Nanofluids containing MWCNTs coated

with nitrogen-rich plasma polymer films for CO₂ absorption in aqueous medium. *Plasma Processes Polym* 2015;12:1311–21.

[26] Olle B, Bucak S, Holmes TC, Bromberg L, Hatton TA, Wang DIC. Enhancement of oxygen mass transfer using functionalized magnetic nanoparticles. *Ind Eng Chem Res* 2006;45:4355–63.

[27] Irani V, Tavasoli A, Vahidi M. Preparation of amine functionalized reduced graphene oxide/methyl diethanolamine nanofluid and its application for improving the CO₂ and H₂S absorption. *J Colloid Interface Sci* 2018;527:57–67.

[28] Yao D, Li T, Zheng Y, Zhang Z. Fabrication of a functional microgel-based hybrid nanofluid and its application in CO₂ gas adsorption. *React Funct Polym* 2019;136:131–7.

[29] Golkhar A, Keshavarz P, Mowla D. Investigation of CO₂ removal by silica and CNT nanofluids in microporous hollow fiber membrane contactors. *J Membr Sci* 2013;433:17–24.

[30] Kim DK, Mikhaylova M, Zhang Y, Muhammed M. Protective coating of superparamagnetic iron oxide nanoparticles. *Chem Mater* 2003;15:1617–27.

[31] Hui C, Shen C, Tian J, Bao L, Ding H, Li C, et al. Core-shell Fe₃O₄@SiO₂ nanoparticles synthesized with well-dispersed hydrophilic Fe₃O₄ seeds. *Nanoscale* 2011;3:701–5.

[32] Arshadi M, Eskandarloo H, Karimi Abdolmaleki M, Abbaspourrad A. A biocompatible nanodendrimer for efficient adsorption and reduction of Hg(II). *ACS Sustain Chem Eng* 2018;6:13332–48.

[33] Arshadi M, Foroughifar S, Etemad Gholtash J, Abbaspourrad A. Preparation of iron nanoparticles-loaded Spondias purpurea seed waste as an excellent adsorbent for removal of phosphate from synthetic and natural waters. *J Colloid Interface Sci* 2015;452:69–77.

[34] Azadbakht T, Zolfogol MA, Azadbakht R, Khakyzadeh V, Perrin DM. C(sp₂)-C(sp₂) cross coupling reaction catalyzed by a water-stable palladium complex supported onto nanomagnetic particles. *New J Chem* 2015;39:439–44.

[35] Arshadi M, Abdolmaleki MK, Eskandarloo H, Azizi M, Abbaspourrad A. Synthesis of highly monodispersed, stable, and spherical NZVI of 20–30 nm on filter paper for the removal of phosphate from wastewater: batch and column study. *ACS Sustain Chem Eng* 2018;6:11662–76.

[36] Selig MJ, Mehrad B, Zamani H, Kierulf A, Licker J, Abbaspourrad A. Distribution of oil solubilized β -carotene in stabilized locust bean gum powders for the delivery of orange colorant to food products. *Food Hydrocolloids* 2018;84:34–7.

[37] Babamiri B, Hallaj R, Salimi A. Ultrasensitive electrochemiluminescence immunoassay for simultaneous determination of CA125 and CA15-3 tumor markers based on PAMAM-sulfanilic acid-Ru(bpy)₃²⁺ and PAMAM-CdTe@CdS nanocomposite. *Biosens Bioelectron* 2018;99:353–60.

[38] Kierulf A, Azizi M, Eskandarloo H, Whaley J, Liu W, Perez-Herrera M, et al. Starch-based Janus particles: Proof-of-concept heterogeneous design via a spin-coating spray approach. *Food Hydrocolloids* 2019;91:301–10.

[39] Arshadi M, Mousavini F, Khalafi-Nezhad A, Firouzabadi H, Abbaspourrad A. Adsorption of mercury ions from wastewater by a hyperbranched and multi-functionalized dendrimer modified mixed-oxides nanoparticles. *J Colloid Interface Sci* 2017;505:293–306.

[40] Arshadi M, Mousavini F, Abdolmaleki MK, Amiri MJ, Khalafi-Nezhad A. Removal of salicylic acid as an emerging contaminant by a polar nano-dendritic adsorbent from aqueous media. *J Colloid Interface Sci* 2017;493:138–49.

[41] Azizi M, Kierulf A, Connie Lee M, Abbaspourrad A. Improvement of physico-chemical properties of encapsulated echium oil using nanostructured lipid carriers. *Food Chem* 2018;246:448–56.

[42] Abboud M, Youssef S, Podlecki J, Habchi R, Germanos G, Foucaran A. Superparamagnetic Fe₃O₄ nanoparticles, synthesis and surface modification. *Mater Sci Semicond Process* 2015;39:641–8.

[43] Bai H, Zheng Y, Wang T, Peng N. Magnetic solvent-free nanofluid based on Fe₃O₄/polyaniline nanoparticles and its adjustable electric conductivity. *J Mater Chem A* 2016;4:14392–9.

[44] Hong R-Y, Li J-H, Zhang S-Z, Li H-Z, Zheng Y, J-m Ding, et al. Preparation and characterization of silica-coated Fe₃O₄ nanoparticles used as precursor of ferrofluids. *Appl Surf Sci* 2009;255:3485–92.

[45] Zhang S, Zhang Y, Liu J, Xu Q, Xiao H, Wang X, et al. Thiol modified Fe₃O₄@SiO₂ as a robust, high effective, and recycling magnetic sorbent for mercury removal. *Chem Eng J* 2013;226:30–8.

[46] Jiang Y, Jiang Z-J, Yang L, Cheng S, Liu M. A high-performance anode for lithium ion batteries: Fe₃O₄ microspheres encapsulated in hollow graphene shells. *J Mater Chem A* 2015;3:11847–56.

[47] Fang X, Xuan Y, Li Q. Experimental investigation on enhanced mass transfer in nanofluids. *Appl Phys Lett* 2009;95:203108.

[48] Eby DM, Artyushkova K, Paravastu AK, Johnson GR. Probing the molecular structure of antimicrobial peptide-mediated silica condensation using X-ray photoelectron spectroscopy. *J Mater Chem* 2012;22:9875–83.

[49] Nabipour M, Keshavarz P, Raeissi S. Experimental investigation on CO₂ absorption in Sulfonol-M based Fe₃O₄ and MWCNT nanofluids. *Int J Refrig* 2017;73:1–10.

[50] Lee JW, Jung J-Y, Lee S-G, Kang YT. CO₂ bubble absorption enhancement in methanol-based nanofluids. *Int J Refrig* 2011;34:1727–33.

[51] Parvazinia M, Garcia S, Maroto-Valer M. CO₂ capture by ion exchange resins as amine functionalised adsorbents. *Chem Eng J* 2018;331:335–42.

[52] Kim S, Ida J, Giulians VV, Lin YS. Tailoring pore properties of MCM-48 silica for selective adsorption of CO₂. *J Phys Chem B* 2005;109:6287–93.

[53] Kim JH, Jung CW, Kang YT. Mass transfer enhancement during CO₂ absorption process in methanol/Al₂O₃ nanofluids. *Int J Heat Mass Transf* 2014;76:484–91.

[54] Sundar LS, Sharma KV, Naik MT, Singh MK. Empirical and theoretical correlations on viscosity of nanofluids: a review. *Renew Sustain Energy Rev* 2013;25:670–86.

[55] Jung J-Y, Lee JW, Kang YT. CO₂ absorption characteristics of nanoparticle suspensions in methanol. *J Mech Sci Technol* 2012;26:2285–90.

[56] Krishnamurthy S, Bhattacharya P, Phelan PE, Prasher RS. Enhanced mass transport in nanofluids. *Nano Lett* 2006;6:419–23.

[57] Turanov AN, Tolmachev YV. Heat- and mass-transport in aqueous silica nanofluids. *Heat Mass Transf* 2009;45:1583–8.

[58] Zhang G, Zhao P, Hao L, Xu Y. Amine-modified SBA-15(P): a promising adsorbent for CO₂ capture. *J CO₂ Util* 2018;24:22–33.

[59] Foo GS, Lee JJ, Chen C-H, Hayes SE, Sievers C, Jones CW. Elucidation of surface species through *In Situ* FTIR spectroscopy of carbon dioxide adsorption on amine-grafted SBA-15. *ChemSusChem* 2017;10:266–76.

[60] Wilfong WC, Srikanth CS, Chuang SSC. *In Situ* ATR and DRIFTS studies of the nature of adsorbed CO₂ on tetraethylenepentamine films. *ACS Appl Mater Interfaces* 2014;6:13617–26.

[61] Gao W, Zhou T, Wang Q. Controlled synthesis of MgO with diverse basic sites and its CO₂ capture mechanism under different adsorption conditions. *Chem Eng J* 2018;336:710–20.

[62] Boot-Handford ME, Abanades JC, Anthony EJ, Blunt MJ, Brandani S, Mac Dowell N, et al. Carbon capture and storage update. *Energy Environ Sci* 2014;7:130–89.

[63] Robinson K, McCluskey A, Attalla MI. An ATR-FTIR study on the effect of molecular structural variations on the CO₂ absorption characteristics of heterocyclic amines, Part II. *ChemPhysChem* 2012;13:2331–41.

[64] Li SH, Ding Y, Zhang XS. Enhancement on CO₂ bubble absorption in MDEA solution by TiO₂ nanoparticles. *Adv Mater Res* 2013;631–632:127–34.

[65] W-g Kim, Kang HU, K-m Jung, Kim SH. Synthesis of silica nanofluid and application to CO₂ absorption. *Sep Sci Technol* 2008;43:3036–55.

[66] Jorge L, Coulombe S, Girard-Lauriault P-L. Nanofluids containing MWCNTs coated with nitrogen-rich plasma polymer films for CO₂ absorption in aqueous medium. *Plasma Process Polym* 2015;12:1311–21.

[67] Jung J-Y, Lee JW, Yong TK. CO₂ absorption characteristics of nanoparticle suspensions in methanol. *J Mech Sci Technol* 2012;26:2285–90.

[68] Ma X, Su F, Chen J, Bai T, Han Z. Enhancement of bubble absorption process using a CNTs-ammonia binary nanofluid. *Int Commun Heat Mass Transfer* 2009;36:657–60.

[69] Lee JW, Kang YT. CO₂ absorption enhancement by Al₂O₃ nanoparticles in NaCl aqueous solution. *Energy* 2013;53:206–11.

[70] Taheri M, Mohebbi A, Hashemipour H, Rashidi AM. Simultaneous absorption of carbon dioxide (CO₂) and hydrogen sulfide (H₂S) from CO₂-H₂S-CH₄ gas mixture using amine-based nanofluids in a wetted wall column. *J Nat Gas Sci Eng* 2016;28:410–7.

[71] Torres Pineda I, Lee JW, Jung I, Kang YT. CO₂ absorption enhancement by methanol-based Al₂O₃ and SiO₂ nanofluids in a tray column absorber. *Int J Refrig* 2012;35:1402–9.

[72] Peyravi A, Keshavarz P, Mowla D. Experimental investigation on the absorption enhancement of CO₂ by various nanofluids in hollow fiber membrane contactors. *Energy Fuels* 2015;29:8135–42.